Conditions of appearance and dynamics of the modified two-stream instability in E x B discharges

Federico Petronio, Antoine Tavant, Thomas Charoy, Alejandro Alvarez-Laguna, Anne Bourdon, Pascal Chabert

Conditions of appearance and dynamics of the modified two-stream instability in E × B discharges

Cite as: Phys. Plasmas **28**, 043504 (2021); https://doi.org/10.1063/5.0046843
Submitted: 08 February 2021 . Accepted: 02 April 2021 . Published Online: 29 April 2021

Federico Petronio, Antoine Tavant, Thomas Charoy, Alejandro Alvarez Laguna, Anne Bourdon, and Pascal Chabert

Physics of Plasmas ARTICLE scitation.org/journal/php

Conditions of appearance and dynamics of the modified two-stream instability in E × B discharges

Cite as: Phys. Plasmas **28**, 043504 (2021); doi: 10.1063/5.0046843
Submitted: 8 February 2021 · Accepted: 2 April 2021 ·
Published Online: 29 April 2021

View Online Export Citation CrossMark

Federico Petronio,[1,2,a)] Antoine Tavant,[1] Thomas Charoy,[1] Alejandro Alvarez Laguna,[1] Anne Bourdon,[1] and Pascal Chabert[1]

AFFILIATIONS

[1]Laboratoire de Physique des Plasmas (LPP), CNRS, Sorbonne Université, École Polytechnique, Institut Polytechnique de Paris, 91120 Palaiseau, France
[2]Safran Aircraft Engines, Electric Propulsion Unit, 27208 Vernon, France

[a)]**Author to whom correspondence should be addressed:** federico.petronio@lpp.polytechnique.fr

ABSTRACT

The large differential drift motion between electrons and ions that is created by the E × B current can produce different instabilities, such as the electron cyclotron drift instability, perpendicular to the magnetic field, and the Modified Two-Stream Instability (MTSI), with a component along the magnetic field. In this paper, we derive and validate a stability condition for the apparition of the MTSI modes in 2D particle-in-cell simulations of E × B discharges in the radial-azimuthal plane of a Hall thruster. We verify that, by choosing properly the domain dimensions, it is possible to capture correctly the MTSI growth and its corresponding number of azimuthal periods. In particular, we show that an azimuthal length that is smaller than a certain threshold prevents the MTSI from growing. Moreover, we show that the MTSI growth does not depend on the plasma density, but is affected by the axial electric field (perpendicular to the simulation domain). Additionally, we show that during its linear growth in the early times of the simulations, the MTSI produces an enhanced heating of the electrons in the magnetic field direction as well as an increased cross field mobility. For longer times, in the nonlinear regime, the system evolves toward a more chaotic state with the presence of structures that mostly exhibit large azimuthal wavelengths.

I. INTRODUCTION

Partially magnetized **E** × **B** discharges are widely used in plasma-based technologies, from magnetron reactors for sputter deposition to Hall Effect Thrusters (HETs) for electric propulsion. In these discharges, a magnetic field perpendicular to the electric field is imposed with a design such that the electrons are magnetized whereas the ions remain unmagnetized. This magnetic field is used to increase the residence time of the electrons in the discharge as they remain trapped in the magnetic field lines and form a current in the **E** × **B** direction. However, the presence of the large drift motion between electrons and ions results in microinstabilities that reduce the electron confinement and, ultimately, modify the discharge properties. The impact of the plasma microinstabilities on the transport is referred to as anomalous transport (as opposed to the classical transport caused by particle collisions). Despite the efforts through theoretical and numerical studies, the anomalous transport in **E** × **B** discharges remains currently poorly understood. The Electron Cyclotron Drift Instability (ECDI) was invoked as one of the instabilities responsible for the anomalous transport.[1,12,18] Different particle-in-cell (PIC) simulations under HET conditions have confirmed the presence of the ECDI in 1D azimuthal (in the **E** × **B** direction),[12,16] 2D radial-azimuthal (**B** and **E** × **B** directions),[17,30] and 2D axial-azimuthal configuration (plane perpendicular to **B**).[6,9,22] In these simulations, the ECDI behaves as an unmagnetized ion-acoustic wave with a component that propagates along the **E** × **B** direction at frequencies of the order of 5 MHz and wavelengths of around 1 mm.

In addition to the ECDI, another type of electrostatic instability that has a component along the magnetic field has been observed in PIC simulations[17] and proposed to play a role in the anomalous transport. This instability is identified as the Modified Two-Stream Instability (MTSI).[26] The MTSI is an electrostatic instability that appears under homogenous plasma conditions (i.e., without density gradients) caused by the **E** × **B** drift between magnetized electrons and unmagnetized ions. As compared to the ECDI, it has lower frequency

and its component along the drift direction appears at longer wavelengths (in HET conditions, approximately 1 MHz and 5 mm). In addition, the MTSI has a component along the magnetic field, unlike the ECDI that is completely perpendicular to **B**. The MTSI has been found in simulations of collisionless shocks[26,34] and, more recently, in simulations of $\mathbf{E}\times\mathbf{B}$ discharges.[17,27]

Janhunen *et al.*[17] studied the MTSI under typical HET conditions by calculating the dispersion relation (DR) with unmagnetized ions and magnetized electrons. The MTSI resonance peak was identified at low azimuthal wavenumbers with a radial component. By means of a radial-azimuthal PIC simulation, they studied the MTSI characteristics and its coupling with ECDI modes. Nevertheless, in their work the simulations do not reach a steady state since absorbing walls were used without an ionization source and, hence, the plasma density was decreasing in time.

The presence of the MTSI in HETs is still not well understood as it has only been observed recently[17,31] and not in previous radial-azimuthal PIC simulations.[10,11,14,15,33] The numerical noise due to a poor particle resolution was invoked as a possible explanation for this disagreement.[16] However, a recent study has shown that the convergence of PIC simulations with the number of particles in 2D is not as demanding as in 1D.[8] As a consequence, heretofore, there is not full agreement on the conditions for the appearance of the MTSI in 2D $\mathbf{E}\times\mathbf{B}$ PIC simulations and its impact on the discharge at steady state.

In this work, we aim at clarifying the conditions for the development of the MTSI, by comparing the theoretical MTSI dispersion relation with PIC simulations under different setups that are relevant for HET. Through these simulations, we will identify the configurations that favor the growth of the MTSI by changing the azimuthal and radial lengths of the simulation domain, the plasma density, and electric field intensity. As opposed to previous works, we will achieve steady state solutions by using reflecting walls in the radial direction, as previously done by Sengupta and Smolyakov.[30] This allows us to study in detail how the MTSI affects the discharge behavior at steady state and its impact on the electron temperature, axial electron mobility, and k-spectrum.

The organization of the paper is as follows. The physical and numerical models are described in Sec. II, along with the analytical developments to calculate the dispersion relation (DR). In Sec. III, several PIC simulations results are compared to the theoretical DR to understand which configuration favors the growth of the MTSI. Finally, the influence of the MTSI on the discharge behavior is studied in Sec. IV.

II. MODELS

A. Particle-in-cell simulations

In this work, we use a 2D-3V PIC code, *LPPic*, that has been extensively used for HET simulations[10,32] and benchmarked in a 2D $\mathbf{E}\times\mathbf{B}$ configuration.[8] Here, we simulate the radial-azimuthal plane of a HET with a 2D Cartesian mesh. A magnetic field **B** is imposed in the radial z direction while an electric field **E** is imposed in the axial x direction, which is perpendicular to the simulation plane. The plasma is assumed to be composed of only singly charged xenon ions and magnetized electrons. The geometry is simplified in the azimuthal direction, neglecting the curvature, with an azimuthal domain length L_y that is around ten times smaller than the real thruster circumference that measures ∼20 cm. Periodic boundary conditions are considered in the azimuthal direction. Figure 1 shows a schematic representation of the simulation domain.

In the radial direction, the domain is bounded by two reflecting walls at a fixed potential $\phi = 0$. At the reflecting walls, the particles impinging the boundary are reflected specularly, as done previously in Refs. 28 and 30. The use of these boundaries has two major advantages. (i) A steady state is reached without the need of an artificial reinjection of particles, which may impact the development of the instabilities. The mean plasma density remains constant throughout the simulation, whereas the steady state for energy is reached after around 5–10 μs. (ii) The absence of the sheaths simplifies the physics at the system boundaries.

Despite the simulations are in 2D (radial-azimuthal), the evolution of the plasma in the axial direction is also treated in order to reach a steady state, as explained below. This kind of axial virtual model has been widely used before, both in 1D and 2D.[10,11,18] Even though there is only one cell in the axial direction, two boundaries in this direction are considered at $x = 0$ and $x = L_x$. When one particle crosses one of these boundaries, another is re-injected at the other side at the same radial and azimuthal position with a velocity sampled from a Maxwellian flux distribution at the initial temperature. By doing this, the total energy of the plasma saturates after some time, which allows the simulation to reach a steady state.

The physical and numerical parameters, if not otherwise stated, are presented in Table I. The dimensions L_y and L_z will be varied in our study whereas the axial length L_x is fixed to 2 cm. As compared to previous works,[33] in the present paper we aim at studying the evolution of the plasma oscillations with a larger azimuthal domain. Collisional processes and wall secondary-electron emission are not taken into account. As a result, the mean density of electrons and ions remains constant and equal to the initial one during the simulation. The electron–neutral collisions do not interfere with the instability mechanism.[17] Their collision frequency[5] ($\nu_{e,n} \sim 5$ MHz) is below the observed[17] growth rate of MTSI ($\gamma \sim 10$ MHz). The effect of the collisions at steady state is not investigated in this work. Statistical convergence has been tested by increasing the average number of particles

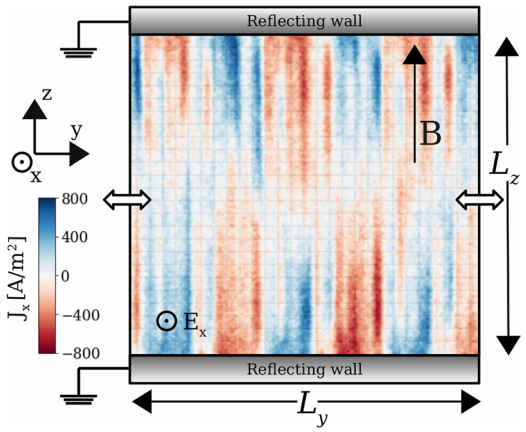

FIG. 1. Schematic representation of the radial-azimuthal (z–y) simulation domain, with periodic boundary conditions in $y-$ direction and two perfectly reflecting walls at the edges of the z one. The snapshot represents the axial current density at 1.5 μs in a simulation domain 1.28 cm × 1.28 cm.

TABLE I. Operating and numerical parameters used in PIC simulations.

Physical parameters	Symbol	Value	Unit
Radial magnetic field	B	200	G
Axial electric field	E_x	1×10^4	V/m
Axial length	L_x	2	cm
Gas		Xenon	$(\cdots)$
Initial plasma density	n_0	5×10^{16}	m^{-3}
Initial electron temperature	T_e	10	eV
Initial ion temperature	T_i	0.5	eV
Neutral pressure	P_n	0	$(\cdots)$
Simulation parameters			
Time step	Δt	1.5×10^{-12}	s
Cell size	$\Delta y = \Delta z$	5×10^{-5}	m
Initial number of particles per cell	N/NG	100	Particles/cell
Number of iterations between outputs	N_a	1000	$(\cdots)$

per cell (N/NG) up to 400, without any major effect on the discharge characteristics.

Numerical parameters have been chosen to satisfy the electrostatic PIC stability conditions,[4] i.e., the cell size Δy and the time step Δt are small enough to resolve the Debye length, $\lambda_D = \sqrt{\epsilon_0 k_B T_e / n_e q_e^2}$ and the electron plasma frequency $\omega_{pe} = \sqrt{n_e q_e^2 / m_e \epsilon_0}$, respectively. Here, ϵ_0 is the vacuum permittivity, k_B the Boltzmann constant, q_e, m_e, n_e, T_e the electron charge, mass, density, and temperature, respectively. It requires approximately ~30 h on 144 CPUs to simulate 10 μs of physical time.

B. Analytic study

The solution of the kinetic dispersion relation at finite temperature does not allow for an analytical expression. For this reason, in this section, from a fluid DR we will derive a simple analytical law that permits to estimate the conditions for the appearance of the MTSI in the PIC simulations.

As in Refs. 17 and 25, we consider a 2D fluid dispersion relation under the hypotheses of unmagnetized ions and magnetized electrons with a Maxwellian velocity distribution, in the limit $T_e \to 0$, as follows:

$$1 - \frac{\omega_{pi}^2}{\omega^2} - \frac{\omega_{pe}^2 k_z^2}{(\omega - k_y v_0)^2 k^2} - \frac{\omega_{pe}^2 k_y^2}{\left((\omega - k_y v_0)^2 - \Omega_{ce}^2\right) k^2} = 0, \quad (1)$$

where $\mathbf{k} = k_y \mathbf{e}_y + k_z \mathbf{e}_z$ is the vectorial wavenumber, $k = |\mathbf{k}|$ is its absolute value, $\omega_{pi} = \sqrt{n_i q_e^2 / m_i \epsilon_0}$ is the ion plasma frequency, $\Omega_{ce} = qB/m_e$ is the electron cyclotron frequency, and v_0 is the electron drift velocity in azimuthal direction. The azimuthal $\mathbf{E} \times \mathbf{B}$ drift reads $\mathbf{v_0} = \frac{\mathbf{E} \times \mathbf{B}}{B^2} = \frac{E}{B} \mathbf{e_y}$.

To solve Eq. (1) numerically, we nondimensionalized the wavenumbers with the inverse of the electron Debye length λ_D, the frequency with the ion plasma frequency, and the velocities by the Bohm speed $u_B = \lambda_D \omega_{pi} = \sqrt{k_B T_e / m_i}$. The dimensionless DR reads

$$1 - \frac{1}{\tilde{\omega}^2} - \frac{m_i}{m_e} \frac{\tilde{k}_z^2}{(\tilde{\omega} - \tilde{k}_y \tilde{v}_0)^2 \tilde{k}^2} - \frac{m_i}{m_e} \frac{\tilde{k}_y^2}{\left((\tilde{\omega} - \tilde{k}_y \tilde{v}_0)^2 - \frac{\Omega_{ce}^2}{\omega_{pi}^2}\right) \tilde{k}^2} = 0, \quad (2)$$

with $\tilde{\omega} = \omega/\omega_{pi}$, $\tilde{k}_j = k_j \lambda_D$, and $\tilde{v}_0 = v_0/u_B$. The reference values are calculated with the conditions of Table I. Note that, in the following, the dimensionless quantities are denoted with a tilde.

The solver uses scipy.optimize,[35] which employs the Nelder–Mead method with the dimensionless convergence tolerance of $\xi = 10^{-12}$. For fixed $\tilde{k}_y$ and $\tilde{k}_z$, we solve for the complex frequency $\tilde{\omega} = \tilde{\omega}_r + i\tilde{\gamma}$, where $\tilde{\gamma} = \gamma/\omega_{pi}$ is the nondimensional growth rate and $\tilde{\omega}_r = \omega_r/\omega_{pi}$ the nondimensional frequency. Figure 2 shows an example of the solution $(\tilde{\gamma}, \tilde{\omega}_r)$ in the $\tilde{k}_y - \tilde{k}_z$ space for the parameters specified above. In the bottom panels of the figure, the solid lines show the solution for the growth rate and frequency as a function of the azimuthal wavenumber for $\tilde{k}_z = 0.02$. The peak represents the MTSI resonance.

The dimensionless DR, i.e., Eq. (2), does not have a trivial analytic solution. However, it can be simplified using the following assumptions. First, in our range of interest we have $\tilde{k}_z \ll \tilde{k}_y$, thus we can consider that $\tilde{k} \approx \tilde{k}_y$. Furthermore, as it is a low-frequency wave, the numerical solution of Eq. (2) verifies the following inequality $\tilde{\omega} \ll \tilde{k}_y \tilde{v}_0$. Finally, in our range of interest the radial wavenumber is such that $\tilde{k}_y \tilde{v}_0 \ll \Omega_{ce}/\omega_{pi}$. For example, in the squared domain shown in Fig. 1, the wavenumbers are $k_z = 245\,\mathrm{m}^{-1}$ and

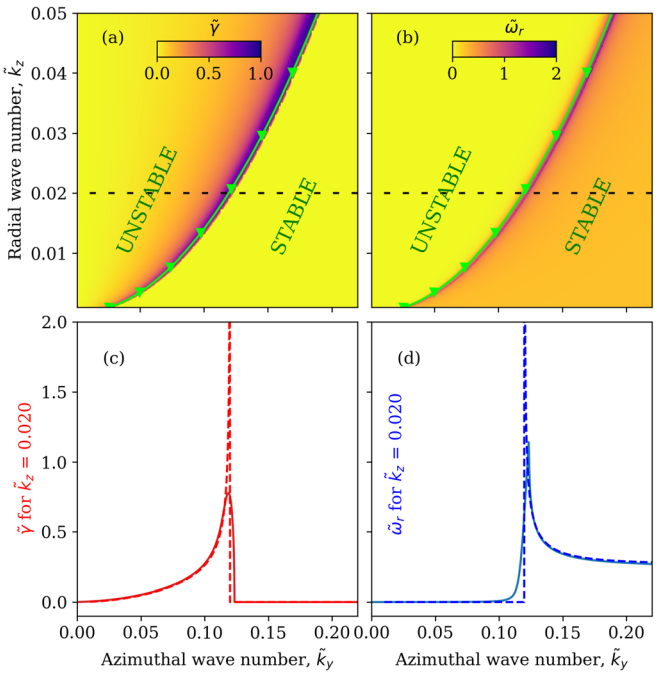

FIG. 2. (a) Phase space of the growth rate $\tilde{\gamma}(\tilde{k}_y, \tilde{k}_z)$; (b) frequency $\tilde{\omega}_r(\tilde{k}_y, \tilde{k}_z)$ as calculated numerically from the dispersion relation in Eq. (2). The green line shows the position of $\max(\tilde{\gamma})$ obtained with the analytical solution of Eq. (5). The black dashed lines in (a) and (b) show the cuts reported in (c) and (d) for, respectively, the growth rate and the frequency. In (c) and (d), the full lines are obtained solving numerically Eq. (2), while the dashed lines are obtained from Eq. (4).

$k_y = 1473\ \mathrm{m}^{-1}$, normalized by the Debye length to $\tilde{k}_z = 0.0258$ and $\tilde{k}_y = 0.1548$. For the same case, we have $\Omega_{ce}/\omega_{pi} \sim 137$, $\tilde{k}_y\tilde{v}_0 \sim 29$ and $\tilde{\omega} \sim 1$. Consequently, we further simplify the denominator of the fourth term. As a result, we obtain a simplified DR that reads

$$1 - \frac{1}{\tilde{\omega}^2} - \frac{m_i}{m_e}\frac{\tilde{k}_z^2}{\tilde{k}_y^4\tilde{v}_0^2} + \frac{m_i}{m_e}\frac{\omega_{pi}^2}{\Omega_{ce}^2} = 0. \tag{3}$$

The explicit solution for $\tilde{\omega}$ can be analytically calculated as

$$\tilde{\omega} = \left[1 + \frac{m_i}{m_e}\frac{\omega_{pi}^2}{\Omega_{ce}^2} - \frac{m_i}{m_e}\frac{\tilde{k}_z^2}{\tilde{k}_y^4\tilde{v}_0^2}\right]^{-\frac{1}{2}}, \tag{4}$$

with a singularity at

$$\tilde{k}_z = \left(\frac{m_e}{m_i} + \frac{\omega_{pi}^2}{\Omega_{ce}^2}\right)^{\frac{1}{2}}\tilde{v}_0\tilde{k}_y^2.$$

Considering that $m_e/m_i \ll \omega_{pi}^2/\Omega_{ce}^2$, the previous expression in dimensional form reads

$$k_z = \frac{m_e E_x}{eB^2}k_y^2. \tag{5}$$

This equation gives the position of maximum growth rate, γ_{MAX}, in the $k_y - k_z$ space. Note that the spectral position of the MTSI resonance, γ_{MAX}, does not depend on the ion mass nor the plasma density, but only on the axial electric field and the radial magnetic field.

In the upper panel of Fig. 2, the position of the maximum growth rate as calculated with the simple relation of Eq. (5) is shown with a green line with triangular markers, delimiting the stable and unstable regions. One can note that this solution is in very good agreement with the position found with the numerical solution of Eq. (2). A comparison of the growth rate and frequency of both the simplified (dashed lines) and the full fluid solution (solid lines) for $\tilde{k}_z = 0.2$ is shown in the panels (c) and (d) of Fig. 2. Note that in the vicinity of the MTSI resonance peak, the approximation $\tilde{\omega} \ll \tilde{k}_y\tilde{v}_0$ is not valid anymore and the simplified formula fails to capture the magnitude of the peak. Nevertheless, Eq. (5) remains a good approximation to identify the position of the MTSI peak in the $k_y - k_z$ space.

As a result of these observations, from Eq. (5), we can establish an analytical stability condition for the appearance of the MTSI in our PIC simulations. The unstable region in the $k_y - k_z$ space fulfills the following condition:

$$k_z \geq \frac{m_e E_x}{eB^2}k_y^2. \tag{6}$$

The boundary conditions of the PIC simulation define a discrete set of couples (k_y, k_z) in the unstable region, as explained below. In our case, the azimuthal wavenumber is fixed by the periodic boundary conditions as $k_y = 2\pi m/L_y$ where m is a positive integer. Similarly, the Dirichlet boundary conditions for the electric potential allow the growth of instabilities with $k_z = p\pi/L_z$ where p is a positive integer. Consequently, the stability condition for our PIC setup can be expressed as

$$L_z/p \leq \frac{eB^2}{4\pi m_e E_x}(L_y/m)^2. \tag{7}$$

The (m, p) couple corresponding to the mode with largest growth rate will likely be the one that develops in the PIC simulation. One should note that the growth rate shown in Fig. 2 is obtained with a fluid DR which overestimates the growth rate at small radial wavelengths. In the kinetic dispersion relation,[17] the growth rate decreases at large radial wavenumbers and, hence, the modes with small wavenumbers are more likely to appear. Under typical HET conditions, this implies that the p with larger growth rate is $p = 1$, which corresponds to half wavelength in the radial direction. Eventually, under certain conditions, $p = 2$ can appear, which corresponds to one wavelength in the radial direction. Modes with larger p, although they are unstable, have a growth rate that is too small as compared to other instabilities. In Sec. III B, these results will be compared to PIC simulations.

C. Methods

Different electrostatic modes, namely, the ECDI and MTSI, can appear simultaneously in our PIC simulations. In order to study separately their characteristics in the 2D PIC simulations, we use here 2D discrete fast Fourier transforms (FFT) of the azimuthal electric field E_y. The FFT is calculated both in the $k_y - k_z$ and in the $k_y - \omega$ phase spaces.

In order to get the MTSI growth rate γ^{PIC}, we calculate the FFT of E_y at every $N_a = 1000$ time steps, obtaining a 2D $k_y - k_z$ map. Once the ECDI and MTSI modes are identified in the map, we determine the MTSI amplitude in the spectrum and we plot it as a function of time. We determine its growth rate γ^{PIC} with a linear regression of the MTSI mode amplitude. Similarly, for the MTSI frequency ω_r^{PIC}, we use a FFT in the $k_y - \omega$ plane, at the radial position $z = L_z/4$. In order to avoid the chaotic nonlinear part of the simulation, we perform the FFT on an interval of 2 μs starting when the MTSI starts to grow. However, this time corresponds to only two or three periods of the MTSI, which results in a rough estimation of ω_r^{PIC}.

The MTSI has been observed to cause a significant heating in the radial direction.[17,26] In this work, we will study the evolution of the mean radial electron temperature, $T_{e,z}$, that is computed at each grid point from the second moment of the distribution function and averaged over the whole simulation domain.

III. STUDY OF THE ON-SET OF THE MTSI IN PIC SIMULATIONS

In Sec. II B, we have proposed an analytical expression to locate the MTSI resonance peak in the wavenumber phase space. Here, these results are compared to 2D radial-azimuthal PIC simulations in order to identify in which configurations the MTSI grows. Table II contains a list of all the simulations that are analyzed in this section. We recall that the DR has been calculated in the limit $T_e \to 0$, while the results presented here are obtained at $T_e > 0$. The finite electron temperature may cause a broadening of the MTSI resonance peak, making the condition Eq. (6) less stringent. So, it is possible to observe the MTSI characterized by wavenumbers not verifying this inequality, but such that $k_z \sim \frac{m_e E_x}{eB^2}k_y^2$.

As an example, in Fig. 3, we show the evolution of the electron density during the onset of the ECDI and MTSI for a representative

TABLE II. The simulation cases from 1 to 5 are analyzed in Sec. III A 1, from 6 to 14 in Sec. III A 2 and from 15 to 17 in Sec. III B. The simulations parameters are the ones specified in Table I if not otherwise stated. If present, $\tilde{\gamma}^{PIC}$ and $\tilde{\omega}_r^{PIC}$ represent the growth rate and the frequency of the MTSI, respectively.

Case number	L_y (cm)	L_z (cm)	$\tilde{\gamma}^{PIC}$	$\tilde{\omega}_r^{PIC}$
1	1.28	0.96	0.078	0.366
2	1.28	1.28	0.101	0.366
3	1.28	1.92	0.181	0.244
4	1.28	2.56	0.368	0.366
5	1.28	3.84	0.157	0.366
6	0.24	0.96	No MTSI	
7	0.48	0.96	0.067	0.244
8	0.24	1.28	No MTSI	
9	0.48	1.28	0.162	0.366
10	0.32	1.92	No MTSI	
11	0.64	1.92	0.202	0.244
12	0.32	2.56	No MTSI	
13	0.64	2.56	0.403	0.366
14	2.56	2.56	0.338	0.366
15[a]	0.64	2.56	0.369	0.366
16[b]	0.64	2.56	No MTSI	
17[b]	1.28	2.56	0.444	0.244

[a]Initial density, $n_0 = 2 \times 10^{17}$ m^{-3}.
[b]Axial electric field, $E_x = 3 \times 10^4$ V/m.

case (case No. 3). As it can be seen, the two modes mainly propagate in the azimuthal direction: one at small wavelength and high frequency which corresponds to the ECDI and another one at larger wavelength that correspond to the MTSI. As the growth rate of the ECDI is larger, it appears first, whereas the MTSI is visible after ~1 μs. As it can be noted, the MTSI mode has a radial component, while ECDI does not. Specular reflection at the walls prevents the formation of the sheaths, which helps to estimate the wavenumber k_z of the MTSI mode along the magnetic field direction (z). In most of our simulations, we observed an half-wavelength between the upper and lower

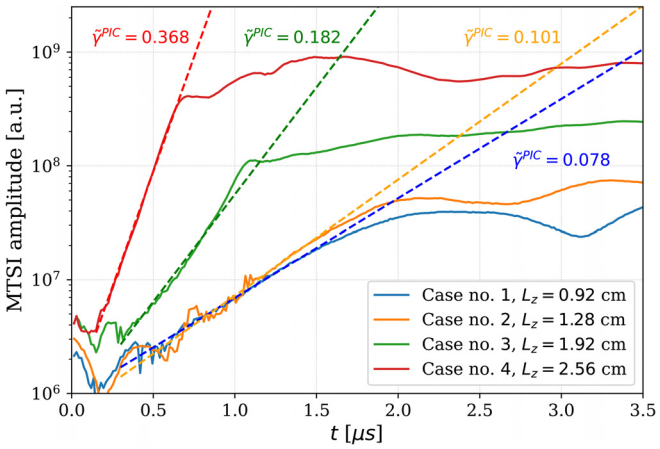

FIG. 4. Evolution of the MTSI amplitude mode calculated from the E_y spectrum of four PIC simulation with different radial lengths. The linear regressions used to calculate $\tilde{\gamma}^{PIC}$ are shown by the dashed lines. The azimuthal length is 1.28 cm for all the cases shown here.

boundaries, with a node at $z = L_z/2$ and two antinodes at $z = 0$ and $z = L_z$, corresponding to a radial wavenumber $k_z = \pi/L_z$. After some microseconds, both oscillations are not in a linear regime, which results in a more chaotic regime with mainly large wavelength structures. In this section, we will primarily focus on the linear regime of the instabilities.

A. Geometric effects

1. Influence of the domain radial length

As explained in Sec. II B, by changing the radial dimension of the simulation domain, the radial wavenumber $k_z = \pi/L_z$ of the MTSI varies. In order to quantify this effect on the instability, we vary the domain radial length L_z from 0.96 cm to 2.56 cm at constant domain azimuthal length $L_y = 1.28$ cm. The temporal evolution of the MTSI amplitude of the azimuthal electric field for four different L_z is shown in Fig. 4. Note that the growth rate of the MTSI is larger for increasing

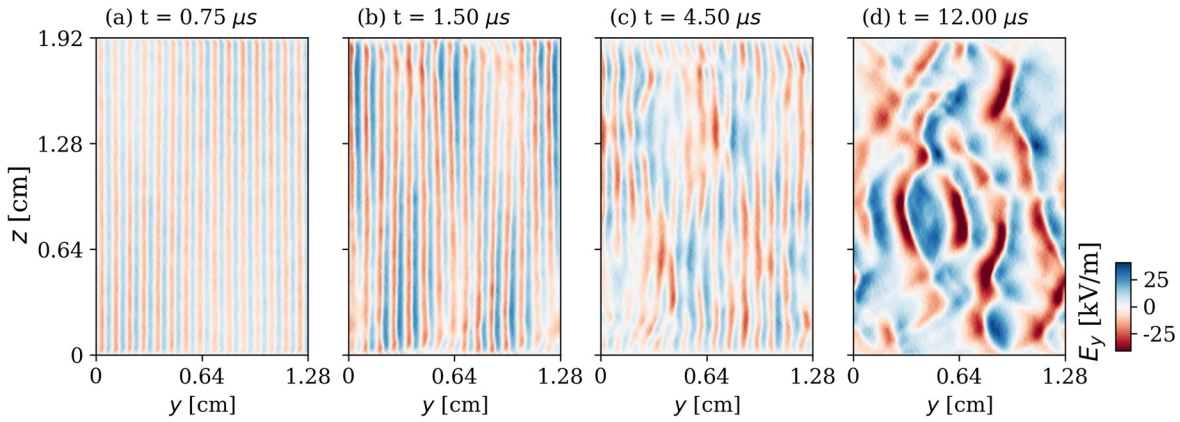

FIG. 3. Snapshots of the azimuthal electric field in case No. 3. In (a), we observe the ECDI. The MTSI appears in (b). Figures (c) and (d) show the transition to a chaotic behavior of the system.

L_z. In addition, the value at which the electric field saturates is also larger for increasing L_z.

In these PIC simulations, the growing modes correspond to the unstable mode, compatible with the PIC boundary conditions, which is the closest to the MTSI peak, as predicted by the analytical formula of Eq. (5). Therefore, Eq. (5) can be regarded as a useful prediction of the wavelength of the fastest growing MTSI. The values of growth rate and frequency resulting from the PIC are different from these calculated with the fluid DR. The reason for this discrepancy can be attributed mainly to the $T_e = 0$ of the fluid DR and other kinetic effects that are present in the PIC simulation. Additionally, the MTSI frequency is inferred at 2 μs after the instability grows, which corresponds only to a few oscillation periods. As the instability grows to a nonlinear regime after few periods, it is difficult to calculate the frequency accurately.

For large enough values of L_z, the largest growing MTSI mode can have an entire wavelength in the radial direction. In Fig. 5, we show two cases with the same azimuthal length and different radial lengths: one with $L_z = 3.84$ cm [case No. 5, shown in panel (a)] and another with half this length [$L_z = 1.92$ cm, case No. 3, shown in panel (c)]. As it can be seen, the case with larger radial length shows an MTSI mode that has an entire wavelength in the radial direction whereas the other case has an MTSI with half wavelength in the radial direction. Interestingly enough, in both cases, the instability has the same k_y and k_z and, as shown in panel (b) of Fig. 5, similar growth rate. The delay in the growth can be due to the random initial distribution of particles.

2. Influence of the domain azimuthal length

As explained in Sec. II B, the periodic boundary conditions in the azimuthal direction play an important role in the selection of the azimuthal wavelength of the MTSI. As a matter of fact, it is possible that the azimuthal length is too small to fit any k_y in the unstable region. This results in a simulation that spuriously do not develop the MTSI, as it will be explained in the following.

The azimuthal boundary conditions select the modes such that $k_y = 2\pi m/L_y$ where m is a positive integer. To illustrate the effect of the azimuthal length on the MTSI, for the set of L_z studied in Sec. III A 1, we perform two different simulations: one with the azimuthal length smaller than the wavelength at the MTSI resonance and another one with the azimuthal length larger than the wavelength at the MTSI resonance. With reference to Table II, we can see that the selection of the azimuthal domain length can have a dramatic influence in the simulation, precluding the formation of the MTSI when it is too small. Conversely, the MTSI in the PIC simulations behave as expected from the DR if the azimuthal domain length is large enough.

The effect of the azimuthal domain length on the instabilities is illustrated in Fig. 6. In this figure, we show 2D snapshots of the azimuthal electric field E_y for three PIC simulations with the same radial length ($L_z = 2.56$ cm) but different azimuthal lengths L_y (from 0.32 cm to 2.56 cm). For too small L_y, only the ECDI develops, while in the other two cases the MTSI is also present. One can note that the same mode of MTSI develops in the cases (b) and (c) of Fig. 6, although more periods of the same wave are captured in the case with larger azimuthal domain.

In Sec. III A 1, we observed that the growth rate strongly depends on the value of the radial wavenumber. Here, we showed that the MTSI can disappear if the azimuthal length is reduced below a certain threshold. Moreover, we observed that once this threshold is reached, the MTSI characteristics (wavelength and growth rate) are not affected if the domain is large enough in the periodic azimuthal direction.

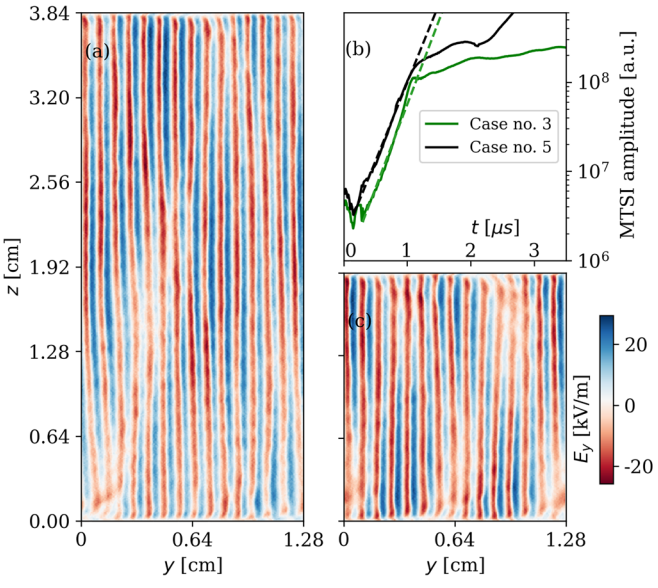

FIG. 5. 2D snapshots ($t = 1.50\,\mu$s) of the azimuthal electric field for (a) $L_z = 3.84$ cm (case No. 5) and (c) $L_z = 1.92$ cm (case No. 3). In (b), evolution of the MTSI mode amplitude in the E_y spectrum. The dashed lines in (b) represent the linear regression calculated during the instability growth.

B. Variation of plasma density and axial electric field

As explained in Sec. II A, the mean plasma density and axial electric field are imposed. Here, as these two parameters vary along the axis of the thruster, we investigate their impact on the MTSI.

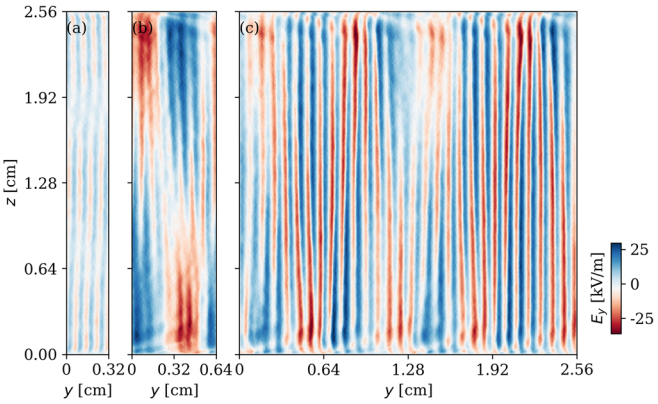

FIG. 6. Snapshots ($t = 1.20\,\mu$s) of E_y for three different PIC simulations with $L_z = 2.56$ cm. (a) $L_y = 0.32$ cm, only ECDI (case No. 12). (b) $L_y = 0.64$ cm, one MTSI period (case No. 13). (c) $L_y = 2.56$ cm, four MTSI periods (case No. 14).

1. Influence of the plasma density

In the simplified dispersion relation, Eq. (4), the dependency of the MTSI dispersion relation on the plasma density is lost. It has been checked with the numerical solution of Eq. (2) that the plasma density has no impact on the MTSI on-set in our $k_y - k_z$ range of interest, under the typical conditions for HETs. This observation has been verified with two PIC simulations with the same geometry: one with the baseline density ($n_0 = 5 \times 10^{16}\,\mathrm{m}^{-3}$, case No. 4) and one with an increased plasma density ($n_0 = 2 \times 10^{17}\,\mathrm{m}^{-3}$, case No. 15).

Figure 7 shows 2D snapshots of the azimuthal electric field for the two PIC simulations: the one with our baseline density in Fig. 7(a) and the one with larger density in Fig. 7(b). We can see that the same long-wavelength MTSI is present for both cases. Moreover, in Fig. 7(c), we observe that the MTSI amplitude evolves with a similar growth rate of $\tilde{\gamma}^{PIC} = 0.369$. These PIC results agree with the conclusion drawn from the analytical dispersion relation: the MTSI does not depend on the plasma density. However, it is important to mention that the ECDI growth rate increases with the plasma density, as expected from Cavalier *et al.*,[7] making more difficult to observe the MTSI in denser plasmas.

2. Influence of the axial electric field

In Eq. (5), we showed that γ_{MAX} has a parabolic shape in $k_y - k_z$ space and that the leading coefficient is proportional to E_x/B^2.

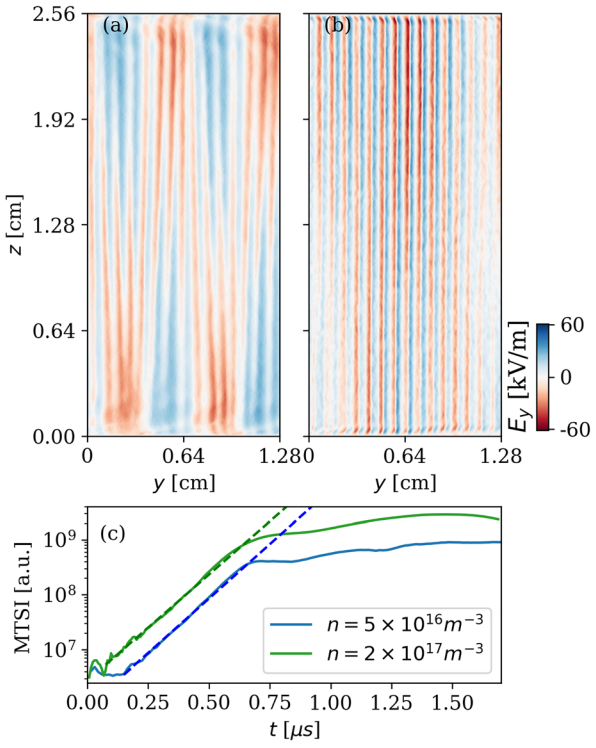

FIG. 7. 2D snapshots ($t = 1.20\,\mu s$) of E_y for (a) the nominal density $n = 5 \times 10^{16}\,\mathrm{m}^{-3}$ (case No. 4) and (b) a larger density $n = 2 \times 10^{17}\,\mathrm{m}^{-3}$ (case No. 15). In (c), evolution of the MTSI mode amplitude in the two cases.

Therefore, the resonance peak depends on the electric and magnetic fields. In this section, we study the impact of varying the axial electric field E_x, with a constant magnetic field.

First, we calculate the DR with different axial electric fields. Figure 8(a) shows the position of the maximum of $\tilde{\gamma}$ for different values of the electric field. Figure 8(b) shows the corresponding growth rate for a fixed radial wavenumber. As the electric field increases, the MTSI peak shifts toward low azimuthal wavenumbers and the growth rate increases. Additionally, we compare the position of γ_{MAX} with the simplified analytical expression of Eq. (5), showing good agreement.

In order to confirm these results with PIC simulations, we compare a case with the baseline electric field $E = 10\,\mathrm{kV/m}$ (case No. 13) with the MTSI to a case with a higher electric field $E = 30\,\mathrm{kV/m}$ (case No. 16). From our previous analytical studies, we expect that no MTSI will grow in the latter case since the MTSI peak is shifted toward smaller k_y and the azimuthal wavelength of the MTSI is too large to fit in the domain. Figures 9(a) and 9(b) show 2D snapshots of the azimuthal electric field corresponding to these two cases. We observe that while the MTSI modulation is clearly visible for the baseline case, we observe only the ECDI for the case with higher axial electric field, as expected. Nevertheless, as explained previously, if L_y is large enough to fit the wavelength of the MTSI, it will appear in our PIC simulation. In Fig. 9(c), we reproduce the simulation at higher electric field with $L_y = 1.28$ cm instead of 0.64 cm. As the domain is large enough to fit the MTSI azimuthal wavelength, the MTSI appears. Additionally, its azimuthal wavelength is approximately twice larger than that in the case with same domain dimensions and baseline electric field [case No. 4, in Fig. 7(a)], which is also in agreement with the prediction in Eq. (5).

C. Summary of results, comparison with previously published results and discussion

In Sec. III, we have extensively studied the linear regime of the MTSI through 2D PIC simulations and compared the results to the

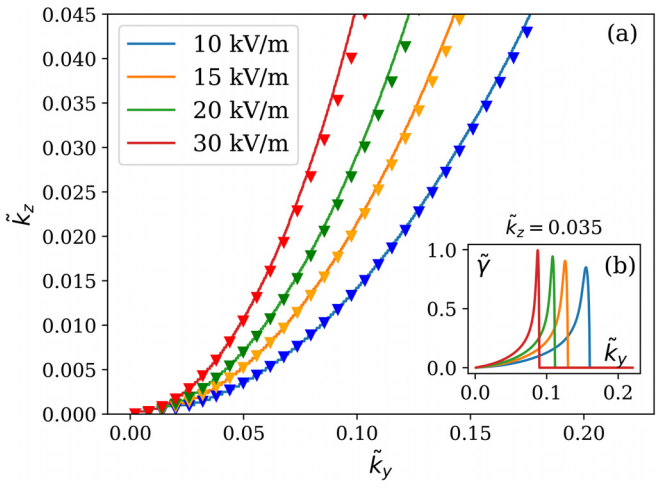

FIG. 8. In (a), the full lines show the position $(\tilde{k}_y, \tilde{k}_z)$ of the maximum of $\tilde{\gamma}$ for different axial electric field calculated from the fluid DR Eq. (2). The ▼ shows the position of γ_{MAX} obtained with the simplified analytical DR Eq. (5). In (b), we show the growth rate $\tilde{\gamma}(\tilde{k}_y)$ for $\tilde{k}_z = 0.035$ for different values of the axial electric field.

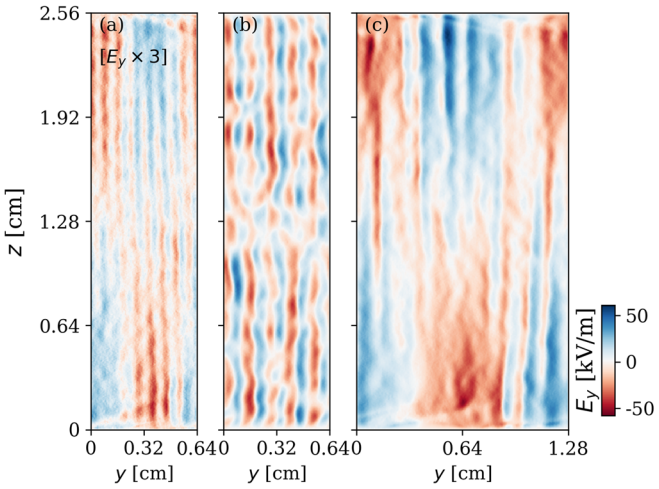

FIG. 9. 2D snapshots ($t = 1.20\,\mu$s) of E_y if (a) $E_x = 10$ kV/m and $L_y = 0.64$ cm (case No. 13), (b) $E_x = 30$ kV/m and $L_y = 0.64$ cm (case No. 16) and (c) $E_x = 30$ kV/m and $L_y = 1.28$ cm (case No. 17). Notice that in (a) E_y is magnified by a factor 3.

analytical expression that was derived in Sec. II B. In Fig. 10, we show a summary of the simulation cases in the (k_y, k_z) phase space together with the position of maximum growth rate as expected with the conditions of Table I. We clearly see that the cases where the MTSI was observed are close to the parabola described in Eq. (5) that delimits the maximum growth rate of the MTSI. Alternatively, the purple bullets represent the allowed couples $(\tilde{k}_y, \tilde{k}_z)$, corresponding to an half-wavelength radially and a single wavelength azimuthally, for the cases

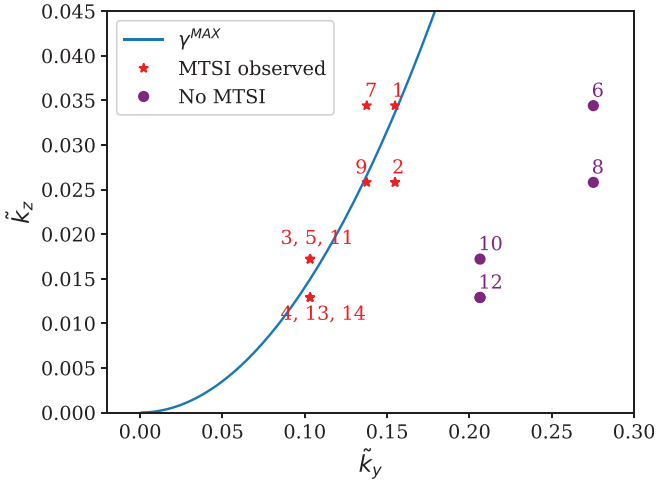

FIG. 10. The blue line shows the instability limit in Eq. (5). The red points represent the couples $(\tilde{k}_y, \tilde{k}_z)$ for which the MTSI is observed. Next to each point, we report the related simulation labels. The purple points represent the allowed couples $(\tilde{k}_y, \tilde{k}_z)$, corresponding to an half-wavelength radially and a single wavelength azimuthally, in the cases where MTSI is not observed. Notice that case Nos. 4, 13, 14 and Nos. 3, 5, 15 correspond to the same point. The details about each simulation are reported in Table II.

where MTSI is not observed. These points are all in the stable region and far from the singularity. Despite there are some of the cases with MTSI that are in a stable region, it is possible that the temperature induces a broadening of the resonance peak, allowing the growth of the MTSI under conditions where the fluid DR with $T_e = 0$ is stable.

In the following, we extend these conclusions to previously published works presenting radial-azimuthal PIC simulations. For this purpose, we consider the conditions used by Tavant *et al.*,[33] where the MTSI was not observed, and these used by Janhunen *et al.*,[17] where the MTSI was reported. In Fig. 11, we show the position of the maximum growth rate, as calculated by the simplified DR, and the explicit resonances allowed by the periodic boundary conditions used in the azimuthal direction. In Figs. 11(a) and 11(c), we see that the k_y allowed by the boundary conditions in Tavant *et al.* is larger than the MTSI resonance peak, which explains why they did not observe any MTSI long-wavelength structures. Alternatively, Janhunen *et al.* observed one MTSI period in the azimuthal direction, which is in perfect agreement with the results of Figs. 11(b) and 11(d) as one of the resonances has a wavelength equal to the value at maximum growth rate.

In conclusion, Eq. (5) is a very useful analytical expression to determine if the PIC domain allows the MTSI to grow. Moreover, it also captures the dependence of the MTSI upon the physical conditions, i.e., density and imposed electric field.

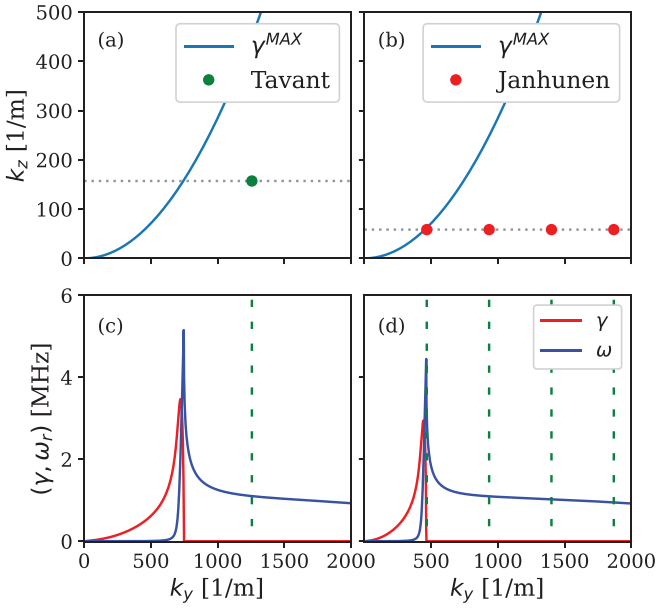

FIG. 11. Positions of the maximum of γ (blue line), calculated with the simplified analytical DR Eq. (5), and allowed (k_y, k_z) (bullet points) using the parameters of (a) Tavant *et al.*[33] (couple with half-wavelength in the radial direction and one in the azimuthal direction) and (b) Janhunen *et al.*[17] (couples for half-wavelength in radial direction and one, two, three and four wavelengths of MTSI in the azimuthal direction). The numerical fluid DR calculated from Eq. (2) for the value of k_z imposed by the boundary conditions is shown for (c) Tavant *et al.*[33] and (d) Janhunen *et al.*[17] The dashed green lines correspond to the allowed k_y, imposed by the periodic boundary conditions. Since the density used in these cases is different, the results are not normalized.

IV. EVOLUTION OF THE PLASMA PROPERTIES WITH THE MTSI

In this section, we study the impact of the MTSI on some macroscopic parameters of the discharge. First, we study the impact on the electron heating in the radial direction. Second, the effect of the MTSI on the anomalous electron mobility in the axial direction. For these studies, we will compare cases with the same radial domain length L_z and two different azimuthal lengths L_y: one that is large enough to capture the MTSI and the other that is too small to develop the MTSI but large enough to capture the ECDI. Finally, we analyze the nonlinear regime in a case with wider azimuthal dimension.

1. Evolution of the electron radial temperature

As noted by McBride,[26] as the MTSI has a radial component, it produces a strong heating in the radial direction. In Fig. 12, we show the evolution of the mean radial temperature $T_{e,z}$ for four cases, two with MTSI (red lines) and two without (blue lines). Note that the reflecting walls are preventing any dissipation of energy in radial direction and, hence, this results in a radial heating in all cases. The saturation of the average energy is obtained only thanks to the axial convection model, as proposed by Lafleur *et al.*[18]

During the transient phase ($0 < t < 4.5\,\mu$s), when the instabilities are easy to distinguish, we can see in Fig. 12 that heating in the radial direction starts much earlier in the cases with MTSI (red lines, case Nos. 11 and 13) than without. Additionally, the case with the largest MTSI growth rate (solid red line) presents the largest heating. Alternatively, in the cases without MTSI (blue lines, case Nos. 10 and 12), the temperature does not depend on the radial length during the transient state. After the linear growth of the MTSI, the system becomes more chaotic and Fig. 12 shows that the electron temperature in the radial direction at saturation is similar in cases with and without MTSI.

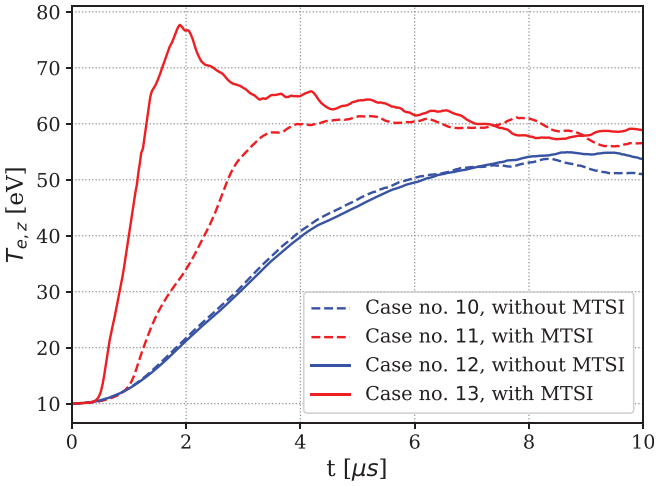

FIG. 12. Evolution of the radial temperature for different PIC simulation cases with: $L_y = 0.64$ cm and $L_z = 1.92$ cm (case No. 10), $L_y = 0.32$ cm and $L_z = 1.92$ cm (case No. 11), $L_y = 0.64$ cm and $L_z = 2.56$ cm (case No. 12), and $L_y = 0.32$ cm and $L_z = 2.56$ cm (case No. 13). The red lines correspond to cases for which the MTSI propagates.

2. Mobility

The axial electron mobility $\mu = -v_x/E_x$, i.e., perpendicular to the y–z simulation plane, is a crucial parameter in HETs. Several studies have been conducted to relate the anomalous mobility and the instabilities propagating in the thruster.[18–22] Recent studies[3,9,21] have observed that the ECDI enhances the transport in axial direction. Here, we show that the long-wavelength MTSI oscillations also contributes to this transport. Following the work of Lafleur *et al.*,[18] it is possible to write the anomalous mobility as a function of the correlation between the oscillations in the azimuthal electric field E_y and the electron density

$$\mu_{eff} = \frac{\frac{|q|}{m\nu_m}}{1+\frac{\Omega_{ce}^2}{\nu_m^2}}\left[1-\frac{\Omega_{ce}\langle\delta n_e \delta E_y\rangle}{\nu_m n_e E_x}\right],$$

where ν_m is the electron–neutral collision frequency. In this work, no collisions are considered. The above equation hence simplifies to

$$\mu_{eff} = -\frac{\langle\delta n_e \delta E_y\rangle}{n_0 E_x B}. \tag{8}$$

To compare the influence of the MTSI on the mobility, we consider two cases, case Nos. 12 and 13, without and with MTSI, respectively, during the transient phase ($0 \le t \le 4.5\,\mu$s) when the instabilities are easy to distinguish. Figures 13(a) and 13(b) show that for the two cases, the measured PIC mobility is in good agreement with the effective mobility given in Eq. (8). We would like to highlight that this definition hence holds even in the presence of MTSI.

In order to understand how the different instabilities affect the mobility, we use a Dynamic Mode Decomposition (DMD),[29] i.e., a data-driven method which identifies the dominant spatial-temporal modes of a signal. This method is applied to the 2D snapshots of the azimuthal electric field and electron density, by using the library Antares.[2] Using this method, the total signal was divided into four frequency packets: the first one contains the low frequency continuous components, the second one gathers the components near the MTSI frequency (between 0.1 and 3 MHz), the third one gathers these near the ECDI frequency (between 3 and 5 MHz), and the fourth one gathers these near to the second resonance of the ECDI frequency (between 5 and 7 MHz). By using this decomposition, we calculated

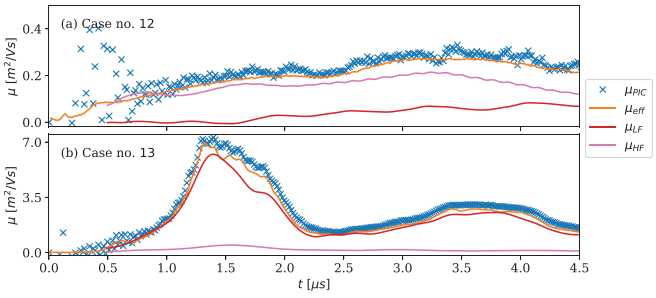

FIG. 13. Axial mean mobility from the PIC (crosses), the correlation term (orange) or the DMD-decomposition (μ_{LF} red, μ_{HF} pink) during the simulation calculated for (a) case No. 12 without MTSI and (b) case No. 13 with MTSI.

the mobility corresponding to each packet using Eq. (8), where μ_{LF} is the mobility related to the range of frequencies around the MTSI and μ_{HF} is this related to ECDI. Figure 13 shows the mobility associated with the different modes for one case without MTSI [case No. 12 shown in panel (a)] and one case with the MTSI [case No. 13 shown in panel (b)]. The mobility related to the second resonance of the ECDI is not shown since it is negligible. We verified in both cases that the sum of μ_{LF} and μ_{HF} corresponds almost perfectly to the measured PIC mobility.

In Fig. 13(a), for the case without MTSI we observe that up to $t = 3\,\mu$s, the main contribution to the mobility μ_{PIC} is due to μ_{HF}, corresponding to the ECDI. For $t > 3\,\mu$s, μ_{LF}, corresponding to the low frequency components traveling at a frequency similar to MTSI start to play a significant role, making more difficult to distinguish the contribution of each mode as the discharge transits to a more chaotic mode. When the MTSI is present, in Fig. 13(b), we note that up to 4.5 μs, the mobility is completely dominated by the MTSI ($\mu \sim \mu_{LF}$). It is interesting to point out that during this transient phase ($0 < t < 4.5\,\mu$s), in the case where the MTSI is present the mobility is one order of magnitude larger than the case without MTSI.

3. Nonlinear regime

Previous works[24] have found that nonlinear effects were playing a major role after some characteristic growth times. In our case, after the linear growth of the instabilities and their saturation, the system becomes more chaotic and the structures cannot anymore be identified as the superposition of only two modes, i.e., ECDI and MTSI.

The energy transition from short- to long-wavelength modes has been predicted theoretically[23] and also observed numerically in 1D and 2D PIC simulations.[16,17] We recall that in our PIC simulations, the total energy is not conserved because the energy is constantly injected by the imposed axial electric field. Therefore, the steady state is reached only thanks to the convection in the virtual axial direction. In Fig. 14(a), we show the k-spectrum of the azimuthal electric field at $z = L_z/2$ for the case No. 3. In the spectrum, for $t < 10\,\mu$s, we can distinguish the MTSI, the ECDI, and the second resonance of the ECDI. At the beginning of the simulation, as the ECDI grows faster, most of the energy is carried by the ECDI, while the intensity of the MTSI is lower. Later, at $t = 10\,\mu$s, we observe a mode transition toward low-k modes with now a negligible quantity of energy carried by the ECDI modes. At this point, we observe a broad spread of the energy over k_y. This time corresponds to a more chaotic state of the system with the presence of structures that mostly exhibit large azimuthal wavelengths.

The spectral analysis in the $\omega - k_y$ phase space provides important insights about the nonlinear state of the system. Lafleur *et al.*[21] suggested that the discrete ECDI transitions to an ion acoustic wave (IAW), due to a resonance broadening mechanism. This has never been studied in the presence of MTSI. The dispersion relation in the IAW limit is given as[19]

$$\omega_r \approx \mathbf{k}\cdot\mathbf{v_i} \pm \frac{kc_s}{\sqrt{1+k\lambda_{D*}}}, \tag{9}$$

$$\gamma = \pm\sqrt{\frac{\pi m_e}{8m_i}}\frac{k_y v_0}{(1+k^2\lambda_{D*}^2)^{3/2}}, \tag{10}$$

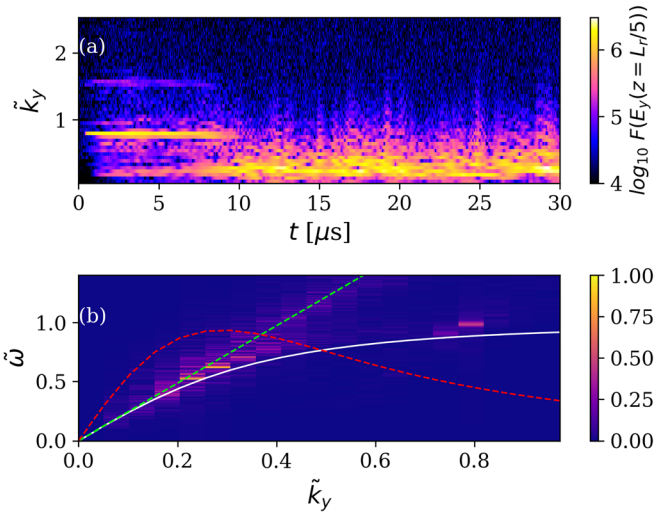

FIG. 14. PIC case No. 3, with $L_y \times L_z = 1.28\,\text{cm} \times 1.92\,\text{cm}$. (a) Time evolution of the k-spectrum of the azimuthal electric field. (b) Normalized plot of the 2D FFT of the azimuthal electric field $E_y(y, z = L_z/2, t)$ with $y \in [0, L_y]$ and $t \in (20\,\mu\text{s}, 30\,\mu\text{s})$. The solid white line shows the ion acoustic dispersion relation in Eq. (9), the dashed line shows the growth rate of the IAW, Eq. (10), magnified 25 times, the green line shows the linear sound relation as in Eq. (12).

where $\mathbf{v_i}$ is the ion drift velocity, $c_s = \sqrt{qT_e/M}$ is the sound speed, and λ_{D*} is the electron Debye length calculated in the nonlinear regime. In the case analyzed here, the ion speed is negligible, thus Eq. (9) simplifies to

$$\omega_r \approx \pm\frac{kc_s}{\sqrt{1+k\lambda_{D*}}}. \tag{11}$$

In the limit $k\lambda_{D*} \ll 1$, the previous equation can be simplified to the linear sound relation between the frequency and the wavenumber

$$\omega_r \approx \pm kc_s. \tag{12}$$

In Fig. 14(b), we show the 2D FFT of the azimuthal electric field at $z = L_z/2$ between 20 and 30 μs for case No. 3. The linear dispersion relation for acoustic waves in Eq. (12) overlaps the observed instability spectrum. Moreover, the dominant wavenumbers observed correspond to the ones with the largest growth rate of Eq. (10). These results show that in the nonlinear regime the perturbations in the electric field travel at the speed of sound; therefore, a saturated IAW might be the dominant mode.

In the nonlinear stage, we do not observe significant variations of the electron temperature and axial mobility. In case No. 3, the mean radial electron temperature grows during the linear regime and remains stable between 20 and 30 μs at ~55 eV with a standard deviation $\sigma = 1.4$ eV. Similarly, in the same time interval, the mobility stabilizes to $\sim 1.4\,\text{m}^2/\text{Vs}$ with fluctuation of the order of $0.2\,\text{m}^2/\text{Vs}$. It is worth remarking that the absolute value of the mobility is considerably lower as compared to the values of $\sim 6\,\text{m}^2/\text{Vs}$ obtained before by Tavant *et al.*[33] with a similar configuration. As they were imposing a higher axial electric field ($E_x = 20\,\text{kV/m}$), their electron drift velocity was higher. The higher v_0 and the larger plasma density

($n_0 = 2 \times 10^{17}\ \mathrm{m}^{-3}$) used in their setup enhance the ECDI oscillations, which could explain their higher axial mobility.

V. CONCLUSION

In this work, we studied the evolution of the Modified Two-Stream Instability (MTSI) in $\mathbf{E} \times \mathbf{B}$ discharge conditions encountered in the radial-azimuthal (z, y) plane of Hall thrusters, by using both theory and numerical simulations. We calculated an approximated version of the fluid dispersion relation of MTSI by Janhunen *et al.*,[17] given by Eq. (3). By solving analytically this simplified dispersion relation, we have identified a stability criterion for the MTSI: the instability grows if one of the couples (k_y, k_z) allowed by the boundary conditions and domain lengths is such that k_z fulfills the condition given by Eq. (6). This analytical criterion has been compared to several 2D PIC simulations of $\mathbf{E} \times \mathbf{B}$ discharges in the radial-azimuthal (z, y) plane of Hall thrusters. We found that the dimensions of the simulation domain play a fundamental role in selecting the values of k_y and k_z. We verified that, by choosing properly the domain dimensions L_y and L_z, it was possible to capture correctly the MTSI growth and its corresponding number of azimuthal periods. In particular, we showed that an azimuthal length that is smaller than a certain threshold prevents the MTSI from growing. Moreover, we showed that the MTSI growth does not depend on the plasma density, but is affected by the axial electric field (the required azimuthal domain L_y for the MTSI to grow is larger for increasing axial electric field). The previous results of Janhunen *et al.*[17] and Tavant *et al.*[33] have been analyzed by using the stability criterion derived in this paper, and we managed to explain the reason why only one MTSI period was observed by the former and why the MTSI was not present in the latter.

We have also studied the impact of the MTSI on the macroscopic variables of the discharge. First, we have observed that during the early times of the simulation when the contribution of different instabilities are easy to distinguish, the MTSI is responsible for a strong heating in the radial direction and enhances the axial electron mobility. For longer times, after the linear growth of the ECDI and MTSI and their saturation, the electric field oscillations are present in a wider spectrum of frequencies and wavelengths. In general, the initial oscillations evolve toward longer azimuthal wavelengths. In this nonlinear regime, we observed some instabilities that are compatible with an ion acoustic mode.

It is important to note that, due to the demanding computational requirements of PIC, the present study is performed in a simplified 2D setup where the collisions with the gas particles and the ionization events where neglected. For this reason, in future work, the use of simulations that account for the gas dynamics, could help to study more consistently the MTSI characteristics for longer time spans. Additionally, all the results in this work are obtained with specular walls. This boundary conditions helped us to compare the simulations with our theoretical developments as the formation of the sheath was prevented. In most of our simulations, we observed a MTSI mode with half wavelength in the radial direction. However, the sheaths allow the growth of modes with a slightly larger value of k_z.[13] Unfortunately, the presence of sheaths prevents from calculating the precise value of k_z, making more difficult the comparison between the PIC results and the fluid DR. The sheaths are expected to change the MTSI radial wavenumber, but the instability criterion is not strongly affected. This fact was verified as we have successfully applied our theory to previous works[17,33] where sheaths were present. Further work is needed in order to investigate the effect of sheaths in the evolution of the MTSI.

ACKNOWLEDGMENTS

F.P. acknowledges the financial support from a Safran Aircraft Engines doctoral research award as well as from the Association Nationale de la Recherche et de la Technologie (ANRT) as part of a CIFRE convention. This work has been partially funded by ANR (No. ANR-16-CHIN-003–01) and Safran Aircraft Engines with the project POSEIDON. This work was granted access to the HPC resources of CINES under the allocation Nos. A0060510439 and A0080510439 made by GENCI.

DATA AVAILABILITY

The data that support the findings of this study are available from the corresponding author upon reasonable request.

REFERENCES

[1]J. C. Adam, A. Héron, and G. Laval, "Study of stationary plasma thrusters using two-dimensional fully kinetic simulations," Phys. Plasmas **11**(1), 295 (2004).
[2]Antares Development Team, Antares Documentation Release 1.15.0, 2012–2020.
[3]Z. Asadi, F. Taccogna, and M. Sharifian, "Numerical study of electron cyclotron drift instability: Application to Hall thruster," Front. Phys. **7**, 140 (2019).
[4]C. K. Birdsall and A. B. Langdon, *Plasma Physics via Computer Simulation* (McGraw-Hill, New York, 1985).
[5]J. P. Boeuf, "Tutorial: Physics and modeling of Hall thrusters," J. Appl. Phys. **121**(1), 011101 (2017).
[6]J. P. Boeuf and L. Garrigues, "E × B electron drift instability in Hall thrusters: Particle-in-cell simulations vs. theory," Phys. Plasmas **25**(6), 061204 (2018).
[7]J. Cavalier, N. Lemoine, G. Bonhomme, S. Tsikata, C. Honoré, and D. Grésillon, "Hall thruster plasma fluctuations identified as the E × B electron drift instability: Modeling and fitting on experimental data," Phys. Plasmas **20**(8), 082107 (2013).
[8]T. Charoy, J. P. Boeuf, A. Bourdon, J. A. Carlsson, P. Chabert, B. Cuenot, D. Eremin, L. Garrigues, K. Hara, I. D. Kaganovich, A. T. Powis, A. Smolyakov, D. Sydorenko, A. Tavant, O. Vermorel, and W. Villafana, "2D axial-azimuthal particle-in-cell benchmark for low-temperature partially magnetized plasmas," Plasma Sources Sci. Technol. **28**(10), 105010 (2019).
[9]T. Charoy, T. Lafleur, A. Tavant, P. Chabert, and A. Bourdon, "A comparison between kinetic theory and particle-in-cell simulations of anomalous electron transport in E × B plasma discharges," Phys. Plasmas **27**(6), 063510 (2020).
[10]V. Croes, "Modélisation bidimensionnelle de la décharge plasma dans un propulseur de Hall," Ph.D. thesis (Université Paris-Saclay, 2017).
[11]V. Croes, T. Lafleur, Z. Bonaventura, A. Bourdon, and P. Chabert, "2D particle-in-cell simulations of the electron drift instability and associated anomalous electron transport in Hall-effect thrusters," Plasma Sources Sci. Technol. **26**(3), 034001 (2017).
[12]A. Ducrocq, J. C. Adam, A. Héron, and G. Laval, "High-frequency electron drift instability in the cross-field configuration of Hall thrusters," Phys. Plasmas **13**(10), 102111 (2006).
[13]S. P. Gary, "Longitudinal waves in a perpendicular collisionless plasma shock: II. Vlasov ions," J. Plasma Phys. **4**(4), 753–760 (1970).
[14]K. Hara, "An overview of discharge plasma modeling for Hall effect thrusters," Plasma Sources Sci. Technol. **28**(4), 044001 (2019).
[15]A. Héron and J. C. Adam, "Anomalous conductivity in Hall thrusters: Effects of the non-linear coupling of the electron-cyclotron drift instability with secondary electron emission of the walls," Phys. Plasmas **20**(8), 082313 (2013).
[16]S. Janhunen, A. Smolyakov, O. Chapurin, D. Sydorenko, I. Kaganovich, and Y. Raitses, "Nonlinear structures and anomalous transport in partially magnetized E × B plasmas," Phys. Plasmas **25**(1), 011608 (2018).
[17]S. Janhunen, A. Smolyakov, D. Sydorenko, M. Jimenez, I. Kaganovich, and Y. Raitses, "Evolution of the electron cyclotron drift instability in two-dimensions," Phys. Plasmas **25**(8), 082308 (2018).

[18]T. Lafleur, S. D. Baalrud, and P. Chabert, "Theory for the anomalous electron transport in Hall effect thrusters. I. Insights from particle-in-cell simulations," Phys. Plasmas **23**(5), 053502 (2016).
[19]T. Lafleur, S. D. Baalrud, and P. Chabert, "Theory for the anomalous electron transport in Hall effect thrusters. II. Kinetic model," Phys. Plasmas **23**(5), 053503 (2016).
[20]T. Lafleur, S. D. Baalrud, and P. Chabert, "Characteristics and transport effects of the electron drift instability in Hall-effect thrusters," Plasma Sources Sci. Technol. **26**(2), 024008 (2017).
[21]T. Lafleur and P. Chabert, "The role of instability-enhanced friction on 'anomalous' electron and ion transport in Hall-effect thrusters," Plasma Sources Sci. Technol. **27**(1), 015003 (2017).
[22]T. Lafleur, R. Martorelli, P. Chabert, and A. Bourdon, "Anomalous electron transport in Hall-effect thrusters: Comparison between quasi-linear kinetic theory and particle-in-cell simulations," Phys. Plasmas **25**(6), 061202 (2018).
[23]V. P. Lakhin, V. I. Ilgisonis, A. I. Smolyakov, and E. A. Sorokina, "Nonlinear excitation of long-wavelength modes in Hall plasmas," Phys. Plasmas **23**(10), 102304 (2016).
[24]M. Lampe, "Theory and simulation of the beam cyclotron instability," Phys. Fluids **15**(4), 662 (1972).
[25]C. Lashmore-Davies and T. Martin, "Electrostatic instabilities driven by an electric current perpendicular to a magnetic field," Nucl. Fusion **13**(2), 193–203 (1973).
[26]J. B. McBride, "Theory and simulation of turbulent heating by the modified two-stream instability," Phys. Fluids **15**(12), 2367 (1972).
[27]I. G. Mikellides and A. L. Ortega, "Growth of the modified two-stream instability in the plume of a magnetically shielded Hall thruster," Phys. Plasmas **27**(10), 100701 (2020).
[28]A. L. Raisanen, K. Hara, and I. D. Boyd, "Two-dimensional hybrid-direct kinetic simulation of a Hall thruster discharge plasma," Phys. Plasmas **26**(12), 123515 (2019).
[29]P. J. Schmid, "Dynamic mode decomposition of numerical and experimental data," J. Fluid Mech. **656**, 5–28 (2010).
[30]M. Sengupta and A. Smolyakov, "Mode transitions in nonlinear evolution of the electron drift instability in a 2D annular E × B system," Phys. Plasmas **27**(2), 022309 (2020).
[31]F. Taccogna, P. Minelli, Z. Asadi, and G. Bogopolsky, "Numerical studies of the E × B electron drift instability in Hall thrusters," Plasma Sources Sci. Technol. **28**(6), 064002 (2019).
[32]A. Tavant, "Plasma-wall interaction and electron transport in Hall effect thrusters," Ph.D. thesis (Université Paris-Saclay, 2019).
[33]A. Tavant, V. Croes, R. Lucken, T. Lafleur, A. Bourdon, and P. Chabert, "The effects of secondary electron emission on plasma sheath characteristics and electron transport in an E × B discharge via kinetic simulations," Plasma Sources Sci. Technol. **27**(12), 124001 (2018).
[34]T. Umeda, Y. Kidani, S. Matsukiyo, and R. Yamazaki, "Modified two-stream instability at perpendicular collisionless shocks: Full particle simulations," J. Geophys. Res. **117**(A3), 017182, https://doi.org/10.1029/2011JA017182 (2012).
[35]P. Virtanen, R. Gommers, T. E. Oliphant, M. Haberland, T. Reddy, D. Cournapeau, E. Burovski, P. Peterson, W. Weckesser, J. Bright, S. J. van der Walt, M. Brett, J. Wilson, K. J. Millman, N. Mayorov, A. R. J. Nelson, E. Jones, R. Kern, E. Larson, C. J. Carey, İ. Polat, Y. Feng, E. W. Moore, J. VanderPlas, D. Laxalde, J. Perktold, R. Cimrman, I. Henriksen, E. A. Quintero, C. R. Harris, A. M. Archibald, A. H. Ribeiro, F. Pedregosa, P. van Mulbregt, and SciPy 1.0 Contributors, "SciPy 1.0: Fundamental algorithms for scientific computing in Python," Nat. Methods **17**, 261–272 (2020).